

Distributions for MSSM Higgs boson + jet production at hadron colliders

OLIVER BREIN ¹ and WOLFGANG HOLLIK ²

¹ *Institute for Particle Physics Phenomenology,
University of Durham, DH1 3LE, Durham, United Kingdom*

² *Max-Planck-Institut für Physik,
Föhringer Ring 6, D-80805 München, Germany*

Abstract

We present pseudorapidity and transverse momentum distributions for the cross section for the production of the lightest neutral Higgs boson in association with a high- p_T hadronic jet, calculated in the framework of the minimal supersymmetric standard model (MSSM). We discuss the theoretical predictions for the differential cross sections at the Large Hadron Collider and the Tevatron for the most common benchmark scenarios.

¹E-mail: obr@mppmu.mpg.de

²E-mail: hollik@mppmu.mpg.de

1 Introduction

The appearance of a light Higgs boson, which might be similar to that of the Standard Model (SM), is a specific feature of the minimal supersymmetric Standard Model (MSSM), and distinguishing the various scenarios is an important task for coming experiments at hadron colliders. Higgs discovery through the main decay channel into a pair of $b\bar{b}$ quarks will be difficult [1], in particular in the mass range below 140 GeV which is common to both the SM and the MSSM, and experimental investigations have to deal with signatures resulting from the more rare decay modes.

Besides inclusive single Higgs production, Higgs boson production in association with a high- p_T hadronic jet provides a useful channel for Higgs searches at hadron colliders, which allows for refined cuts increasing the signal-to-background ratio. Specifically, for the SM Higgs boson [2], simulations considering the decay channels $H \rightarrow \gamma\gamma$ [3, 4] and $H \rightarrow \tau^+\tau^-$ [5] have shown promising signal and background results for the ATLAS detector.

In the meantime, a lot of progress has been made towards improving the SM predictions. The fully differential distribution for Higgs production at next-to-next-to-leading order QCD accuracy has become available [6], improved by resummation of logarithmically enhanced terms for low p_T [7]. Higher-order corrections to differential cross sections for a Higgs boson associated with a high- p_T jet have been obtained explicitly: the next-to-leading order QCD corrections in the large top-mass limit [8] and, recently, the corresponding resummation of soft-gluon emission effects [9].

For the analogous MSSM processes, p_T -distributions have been studied in the limit of vanishing superpartner contributions at leading order [10] and were improved recently by soft-gluon resummation effects [11]. This limit is usually a good approximation when the superpartners are heavy, at a mass scale around 1 TeV. The general case was treated in a previous paper, where we studied the MSSM prediction for the total hadronic cross section for the production of the lightest neutral Higgs boson h^0 in association with a high- p_T jet including all superpartner loop contributions at leading order [12], thus extending the MSSM predictions also to the case of light supersymmetric partners of quarks and gluons.

In the present paper, we complete our study by presenting results for the distributions of pseudorapidity and transverse momentum, η_3 and p_T . Section 2 briefly reviews the contributing parton processes, and Section 3 introduces the expressions for the differential hadronic cross sections $d\sigma/d\eta_3$, $d\sigma/dp_T$ and $d^2\sigma/d\eta_3 dp_T$ in the presence of cuts. In Section 4 we present numerical results for the distributions at the LHC and the Tevatron, based on MSSM parameters around specific benchmark scenarios, in comparison with the SM results.

2 Partonic processes

At the partonic level, production of a Higgs-boson h^0 together with a jet is described generically by

$$P_1(k_1) + P_2(k_2) \rightarrow P_3(k_3) + h^0(k_4),$$

involving partons P_i with momenta $k_i = (E_i, \vec{k}_i)$. There are three classes of parton processes: gluon fusion $g + g \rightarrow g + h^0$ (Figure 1), quark–gluon scattering $q + g \rightarrow q + h^0$ (Figure 2), and quark–anti-quark annihilation $q + \bar{q} \rightarrow g + h^0$ (Figure 3). While gluon fusion is an entirely loop-induced process, the other two classes also get contributions from tree-level b -quark initiated processes (see Figure 4). Those Born-type processes are in general dominant for $m_A \lesssim 120$ GeV, while for large values of m_A the loop-induced processes dominate. This behaviour is essentially a consequence of the Yukawa-coupling of the lightest MSSM Higgs boson to b -quarks, which can be enhanced for low values of the A -boson mass m_A . Formulae for the relevant couplings occurring in this process in our notation can be found in [12, 13].

The virtual presence of the superpartners in the loop contributions modify in addition the overall production rates for supersymmetric Higgs bosons. Moreover, they affect the angular distributions and thus, at the level of hadronic processes, change rapidity and transverse-momentum distributions of the Higgs bosons or the jets, respectively.

In terms of the invariant kinematic variables

$$\hat{s} = (k_1 + k_2)^2, \quad \hat{t} = (k_1 - k_3)^2, \quad (1)$$

the partonic differential cross section reads

$$\frac{d\hat{\sigma}}{d\hat{t}}(\hat{s}, \hat{t}) = \frac{1}{16\pi^2 \hat{s}^2} \overline{|\mathcal{M}(\hat{s}, \hat{t})|^2}, \quad (2)$$

with the spin- and colour-summed/averaged S -matrix element squared.

Instead of \hat{t} , the cross section can be expressed in terms of other variables, such as the transverse momentum $p_T = k_{3,T}$, or the scattering angle $\hat{\theta}$ or rapidity \hat{y}_3 in the parton center-of-mass system (cms), yielding the representations

$$\frac{d\hat{\sigma}}{dp_T}(\hat{s}, p_T) = \frac{d\hat{\sigma}^F}{dp_T}(\hat{s}, p_T) + \frac{d\hat{\sigma}^B}{dp_T}(\hat{s}, p_T), \quad (3)$$

$$\frac{d\hat{\sigma}^{F[B]}}{dp_T}(\hat{s}, p_T) = \frac{2|\vec{k}_1| p_T}{\sqrt{|\vec{k}_3|^2 - p_T^2}} \left. \frac{d\hat{\sigma}}{d\hat{t}}(\hat{s}, \hat{t}) \right|_{\hat{t}=\hat{t}_{F[B]}(\hat{s}, p_T)}, \quad (4)$$

$$\frac{d\hat{\sigma}}{d\hat{\theta}}(\hat{s}, \hat{\theta}) = 2|\vec{k}_1||\vec{k}_3| \sin \hat{\theta} \left. \frac{d\hat{\sigma}}{d\hat{t}}(\hat{s}, \hat{t}) \right|_{\hat{t}=\hat{t}(\hat{s}, \hat{\theta})}, \quad (5)$$

$$\frac{d\hat{\sigma}}{d\hat{y}_3}(\hat{s}, \hat{y}_3) = 2|\vec{k}_1| E_3 (1 - \tanh^2 \hat{y}_3) \left. \frac{d\hat{\sigma}}{d\hat{t}}(\hat{s}, \hat{t}) \right|_{\hat{t}=\hat{t}(\hat{s}, \hat{y}_3)}, \quad (6)$$

with

$$\hat{t}_{F[B]}(\hat{s}, p_T) = -2E_1 E_3 + [-] 2|\vec{k}_1| \sqrt{|\vec{k}_3|^2 - p_T^2}, \quad (7)$$

$$\hat{t}(\hat{s}, \hat{y}_3) = -2E_1 E_3 + 2|\vec{k}_1| E_3 \tanh \hat{y}_3, \quad (8)$$

$$\hat{t}(\hat{s}, \hat{\theta}) = -2E_1 E_3 + 2|\vec{k}_1||\vec{k}_3| \cos \hat{\theta}, \quad (9)$$

$$E_1 = |\vec{k}_1| = \frac{\sqrt{\hat{s}}}{2}, \quad E_3 = |\vec{k}_3| = \frac{\hat{s} - m_h^2}{2\sqrt{\hat{s}}}. \quad (10)$$

3 Hadronic observables

Hadron colliders like the LHC (Tevatron) collide protons with protons (anti-protons) in the center-of-mass system (the laboratory frame) with a total energy \sqrt{S} and individual momenta \vec{P} and $-\vec{P}$, respectively. Hadronic cross section are obtained via convolution of the parton-level cross sections with the parton distributions and summation over the various contributing partons. Experimental restrictions to the detectability of the produced particles are conventionally realized by imposing specific cuts to the kinematically allowed phase space. Typically, cuts are imposed on the final-state transverse momentum and/or the pseudorapidity in order to have high- p_T jets not too close to the beam axis. In our case, we choose the following selection criteria,

$$p_T \equiv |\vec{k}_3| \sin \hat{\theta} > p_T^{\min}, \quad |\eta_3| < \eta_{\max}, \quad (11)$$

where p_T and η_3 denote transverse momentum and pseudorapidity of the final state parton. The first condition leads to an energy cut on the invariant mass of the parton system,

$$\sqrt{\hat{s}} > p_T^{\min} + \sqrt{m_h^2 + (p_T^{\min})^2} \equiv \sqrt{\hat{s}_0}, \quad (12)$$

and to a cut on the scattering angle $\hat{\theta}$ in the parton cms,

$$\sin \hat{\theta} > \frac{2 \hat{s} p_T^{\min}}{\hat{s} - m_h^2}. \quad (13)$$

The second condition in (11) avoids partons with angles θ_{lab} unobservably close to the beam axis in the laboratory frame. For an outgoing massless gluon or quark with momentum k_3 , η_3 coincides with the parton rapidity y_3^{lab} in the laboratory frame, which is related to the rapidity \hat{y}_3 in the parton cms via $\hat{y}_3 = y_3^{\text{lab}} + \psi(\tau, x)$, where ψ is determined by the relative velocity

$$\beta = (x^2 - \tau)/(x^2 + \tau) \equiv -\tanh \psi(\tau, x) \quad (14)$$

of the parton cms with respect to the laboratory frame. Thereby, it is assumed that the initial state partons carry momentum fractions x and τ/x of the hadrons they originate from. The condition $|\eta_3| < \eta_{\max}$ can be written as follows,

$$\arccos(\tanh \eta_{\max}) < \theta_{\text{lab}} < \pi - \arccos(\tanh \eta_{\max}). \quad (15)$$

This translates into the following additional cut on the scattering angle in the parton cms,

$$\hat{\theta}_{\min} \leq \hat{\theta} \leq \hat{\theta}_{\max} \quad (16)$$

with

$$\cos \hat{\theta}_{\min} = \frac{(\tau - x^2) + (\tau + x^2) \tanh \eta_{\max}}{(\tau + x^2) + (\tau - x^2) \tanh \eta_{\max}}, \quad (17)$$

$$\cos \hat{\theta}_{\max} = \frac{(\tau - x^2) - (\tau + x^2) \tanh \eta_{\max}}{(\tau + x^2) - (\tau - x^2) \tanh \eta_{\max}}. \quad (18)$$

Thus, in the additional presence of the pseudorapidity cut the partonic cross section for initial state partons n and m , with momenta $x\vec{P}$ and $-(\tau/x)\vec{P}$, depends on p_T^{\min} , η_{\max} and both variables τ and x ,

$$\hat{\sigma}_{nm}(\tau, x, \eta_{\max}, p_T^{\min}) = \int_{\hat{\theta}_{\min}}^{\hat{\theta}_{\max}} d\hat{\theta} \frac{d\hat{\sigma}_{nm}(\hat{s}, \hat{\theta})}{d\hat{\theta}} \Theta(p_T(\hat{s}, \hat{\theta}) - p_T^{\min}) \Big|_{\hat{s}=\tau S}. \quad (19)$$

3.1 Integrated cross section

The hadronic cross section for h^0 + jet production from two colliding hadrons, A and B , contains the parton densities and the partonic cross sections $\hat{\sigma}_{nm}$ from (19) as follows [14],

$$\begin{aligned} \sigma_{AB}(S, \eta_{\max}, p_T^{\min}) = & \sum_{\{n,m\}} \int_{\tau_0}^1 d\tau \int_{\tau}^1 dx \frac{1}{(1 + \delta_{nm}) x} \times \\ & \left\{ f_{n/A}(x, \mu_F) f_{m/B}\left(\frac{\tau}{x}, \mu_F\right) \hat{\sigma}_{nm}(\tau, x, \eta_{\max}, p_T^{\min}) \right. \\ & \left. + f_{m/A}(x, \mu_F) f_{n/B}\left(\frac{\tau}{x}, \mu_F\right) \hat{\sigma}_{mn}(\tau, x, \eta_{\max}, p_T^{\min}) \right\}, \quad (20) \end{aligned}$$

where $f_{n/A}(x, \mu_F)$ denotes the density of partons of type n in the hadron A carrying a fraction x of the hadron momentum at the factorization scale μ_F [$(A, B) = (p, p)$ for the LHC and (p, \bar{p}) for the Tevatron]. The sum over unordered pairs of incoming partons runs over $\{n, m\} = gg, qq, q\bar{q}$ with the outgoing parton g, q, g respectively, for the various channels. The lower bound of the τ -integration (τ_0) is determined by the minimal invariant mass of the parton system, $\hat{s}_0 = \tau_0 S$, according to (12).

Care has to be taken for the fact that a forward-scattered parton n out of hadron A combines with a backward-scattered parton n out of hadron B or vice-versa to a given value of θ_{lab} or η_3 . Hence, a distinction has to be made in the notation for the integrated partonic cross section: $\hat{\sigma}_{nm}$ has the parton n moving in the direction of the incoming hadron A in the laboratory frame and $\hat{\sigma}_{mn}$ has it in the opposite direction.

3.2 Transverse-momentum distribution

The hadronic cross section differential in p_T is given by the convolution integral of the corresponding partonic differential cross section³,

$$\begin{aligned} \frac{d\sigma_{AB}}{dp_T}(S, p_T, \eta_{\max}) = & \sum_{\{n,m\}} \int_{\tau_0}^1 d\tau \int_{\tau}^1 dx \frac{1}{x} \left\{ \frac{f_{n/A}(x) f_{m/B}\left(\frac{\tau}{x}\right)}{1 + \delta_{nm}} \times \right. \\ & \left. \left[\frac{d\hat{\sigma}_{nm}^F}{dp_T}(\tau S, p_T) \Theta(\eta_{\max} - |\eta_{3,F}^{nm}(\tau, x, p_T)|) \right] + \left[F \leftrightarrow B \right] \right\} + \left\{ m \leftrightarrow n \right\}, \quad (21) \end{aligned}$$

³In the following we drop the factorization scale μ_F in the notation.

with

$$\eta_{3,F[B]}^{nm}(\tau, x, p_T) = -\psi(\tau, x) + [-]\operatorname{arcosh} \frac{\tau S - m_h^2}{2p_T \sqrt{\tau S}}, \quad \eta_{3,F}^{mn} = \eta_{3,B}^{nm}, \quad \eta_{3,B}^{mn} = \eta_{3,F}^{nm},$$

and ψ from (14).

3.3 Pseudorapidity distribution

Taking into account the two directions of motion of the initial state partons in the laboratory system it is convenient to define

$$\hat{y}_3^{nm}(\eta_3, \tau, x) = \eta_3 + \psi(\tau, x), \quad \hat{y}_3^{mn}(\eta_3, \tau, x) = -\hat{y}_3^{nm}(\eta_3, \tau, x). \quad (22)$$

With this convention the formula for the hadronic cross section differential in η_3 reads as follows,

$$\frac{d\sigma_{AB}}{d\eta_3}(S, \eta_3, p_T^{\min}) = \sum_{\{n,m\}} \int_{\tau_0}^1 d\tau \int_{\tau}^1 \frac{dx}{x} \left\{ \frac{f_{n/A}(x) f_{m/B}(\frac{\tau}{x})}{1 + \delta_{nm}} \frac{d\hat{\sigma}_{nm}}{d\hat{y}_3}(\tau S, \hat{y}_3) \Big|_{\hat{y}_3 = \hat{y}_3^{nm}} \Theta(p_T(\tau, x, \eta_3) - p_T^{\min}) + (n \leftrightarrow m) \right\} \quad (23)$$

where

$$p_T(\tau, x, \eta_3) = \frac{\tau S - m_h^2}{2\sqrt{\tau S} \cosh(\eta_3 + \psi(x, \tau))}. \quad (24)$$

3.4 Two-fold differential cross section

The hadronic cross section differential in p_T and η_3 can be written as an integral over a single parameter, which can be chosen to be the parton momentum fraction x . The expression follows from the representation

$$\frac{d^2\sigma_{AB}}{dp_T d\eta_3}(S, \eta_3, p_T) = \sum_{\{n,m\}} \int_{\tau_0}^1 d\tau \int_0^1 \frac{dx}{x} \Theta(x - \tau) G_{nm}(x, \tau, \eta_3) \delta(p_T(\tau, x, \eta_3) - p_T), \quad (25)$$

with

$$G_{nm}(x, \tau, \eta_3) = \frac{f_{n/A}(x) f_{m/B}(\frac{\tau}{x})}{1 + \delta_{nm}} \frac{d\hat{\sigma}_{nm}}{d\hat{y}_3}(\tau S, \hat{y}_3) \Big|_{\hat{y}_3 = \hat{y}_3^{nm}(\eta_3, \tau, x)} + (n \leftrightarrow m), \quad (26)$$

by performing the τ -integration with the help of the δ -function, yielding

$$\frac{d^2\sigma_{AB}}{dp_T d\eta_3}(S, \eta_3, p_T) = \sum_{\{n,m\}} \int_0^1 \frac{dx}{x} \left[\Theta(x - \tau) \Theta(\tau - \tau_0) \frac{x}{\sqrt{S}} \frac{x^2 S e^{-\eta_3} + m_h^2 e^{\eta_3}}{(x\sqrt{S} - p_T e^{\eta_3})^2} G_{nm}(x, \tau, \eta_3) \right]_{\tau=\tau_1(x, \eta_3, p_T)} \quad (27)$$

where

$$\tau_1(x, \eta_3, p_T) = x \left(\frac{x p_T e^{-\eta_3} + \frac{m_h^2}{\sqrt{S}}}{x\sqrt{S} - p_T e^{\eta_3}} \right) \quad (28)$$

fulfils the relation

$$p_T(x, \tau_1, \eta_3) - p_T = 0 \quad (29)$$

with $p_T(x, \tau, \eta_3)$ from (24).

4 Numerical results

In the following discussion we want to illustrate the MSSM predictions for the pseudorapidity and transverse momentum distributions of the hadronic processes $pp \rightarrow h^0 + \text{jet} + X$ and $p\bar{p} \rightarrow h^0 + \text{jet} + X$ and outline differences between MSSM and SM predictions. For comparison of a given MSSM scenario with the SM we choose the SM Higgs mass to have the same value as the h^0 boson in that MSSM scenario. For the numerical evaluation we use the cuts (11) with $p_T^{\text{min}} = 30 \text{ GeV}$ and $\eta_{\text{max}} = 4.5$ as standard cuts, which have been used in previous Standard Model studies for the LHC [3, 4].

The evaluation has been carried out with the MRST parton distribution functions [15], with the renormalisation scale μ_R and factorisation scale for the gluon and the light quarks $\mu_F^{(g)}$ chosen both equal to m_h . For the bottom-quark factorisation scale $\mu_F^{(b)}$ we choose $m_h/4$, inspired by the NNLO prediction for the process $b\bar{b} \rightarrow h^0$ [16] where it proved to be the proper scale choice, as anticipated by several authors [17]. For the strong coupling constant $\alpha_S(\mu_R)$, we use the formula including the two-loop QCD corrections (see e.g. Ref. [18]) for $n_f = 5$ with $\Lambda_{QCD}^5 = 204.8 \text{ MeV}$.

4.1 Parameters

We adopt for our discussion the MSSM benchmark scenarios for the Higgs search at LEP suggested in [19] except for the large- μ scenario which has been ruled out by LEP data [20]. We are interested in effects from the virtual superpartners. Therefore, the no-mixing and m_h^{max} scenario are generalised to have a lower common sfermion mass scale M_{SUSY} than in the original proposal. The two remaining scenarios in [19], the gluophobic and small- α_{eff} scenario, have already a rather low sfermion mass scale.

Although our aim here is mainly exemplary we try to take into account relevant parameter constraints from previous experiments.

Firstly, we calculate for each parameter point the MSSM predictions for m_{h^0} and $\sigma(e^+e^- \rightarrow h^0 Z) \times \text{BR}(h^0 \rightarrow b\bar{b})$ and exclude it if the m_{h^0} -dependent LEP-bound on $\sigma \times \text{BR}$ is violated (according to Table 14(b) of [20]). We use FeynHiggs 2.5.1 [21] for calculating the m_{h^0} prediction and allow for a theoretical uncertainty of 3 GeV.

Secondly, we calculate the leading order MSSM prediction for the branching ratio $\text{BR}(B \rightarrow X_s \gamma)$ [22] and exclude parameter points if the prediction falls outside of the range $(3.55 \pm 1.71) \cdot 10^{-4}$. This range is determined by using the experimental central value [23] and adding up the experimental 3σ interval ($\approx 10^{-4}$) and an estimate of the independent theoretical uncertainty ($0.71 \cdot 10^{-4}$). The latter estimate (20%) is guided by the detailed discussion of theoretical uncertainties for the SM prediction [24].

Furthermore, we took care that all mass exclusion limits from direct search results for superpartner particles [18] are met and that the dominant squark-contribution to the electroweak ρ -parameter [25] stay within ± 0.0025 .

Interestingly, applying the rather conservative bound derived from the $\text{BR}(B \rightarrow X_s \gamma)$ prediction, it turns out that the gluophobic scenario is ruled out in the range we study, $\{m_A \in [50 \text{ GeV}, 1000 \text{ GeV}], \tan \beta \in [1, 50]\}$. For this scenario $\text{BR}(B \rightarrow X_s \gamma)$ is notoriously too large with typical values of the order of 10^{-3} and the lowest value being $7 \cdot 10^{-4}$. We do not include results for this scenario here.

A brief specification of the scenarios investigated is following.

no-mixing(700) scenario : The soft-breaking sfermion mass parameter is set to $M_{\text{SUSY}} = 700 \text{ GeV}$. For M_{SUSY} significantly below 700 GeV the whole range of the m_A - $\tan \beta$ -plane which we study is ruled out. The off-diagonal term $X_t (= A_t - \mu \cot \beta)$ in the top-squark mass matrix is zero, corresponding to a local minimum of m_h as a function of X_t . The supersymmetric Higgsino mass parameter μ is set to -200 GeV , the gaugino mass parameters to $M_1 = M_2 = 200 \text{ GeV}$, and the gluino mass to $M_{\tilde{g}} = 800 \text{ GeV}$. When $\tan \beta$ is changed, A_t is changed accordingly to insure $X_t = 0$. The settings of the other soft-breaking scalar-quark Higgs couplings are $A_b = A_t$ and $A_q = 0$ ($q = u, d, c, s$).

The input for the Higgs sector is specified by $m_A = 500 \text{ GeV}$ and $\tan \beta = 35$.

$m_h^{\text{max}}(400)$ scenario : X_t is set to $2M_{\text{SUSY}}$ which yields the maximal value of m_h with respect to stop mixing effects. We set $M_{\text{SUSY}} = 400 \text{ GeV}$ and the other parameters are chosen as in the previous scenario.

In the $m_h^{\text{max}}(400)$ scenario small values of m_A are still allowed. Hence we examine two Higgs sector scenarios: $m_A = 110 \text{ GeV}$, $\tan \beta = 30$, and $m_A = 400 \text{ GeV}$, $\tan \beta = 30$. The former leads to the dominance of b -quark initiated processes, while the latter is dominated by the loop-induced processes [12].

small- α_{eff} scenario : This scenario gives rise to suppressed branching ratios for the decays $h^0 \rightarrow b\bar{b}$ and $\tau^+ \tau^-$, especially for large $\tan \beta$ and moderate values of m_A . The settings

are: $M_{\text{SUSY}} = 800 \text{ GeV}$, $X_t = -1100 \text{ GeV}$, $M_1 = M_2 = 500 \text{ GeV}$, $\mu = 2000 \text{ GeV}$ and $M_{\tilde{g}} = 500 \text{ GeV}$.

We choose $m_A = 400 \text{ GeV}$ and $\tan\beta = 30$ in the Higgs sector. Values $m_A \lesssim 300$ are already ruled out, and therefore all scenarios with dominance of the b -quark initiated processes as well.

4.2 Differential cross sections at the LHC

The crucial parameter determining the properties of h^0 +jet production in the MSSM is m_A [12]. For $m_A \lesssim 120 \text{ GeV}$ and $\tan\beta$ not too small ($\gtrsim 5$) the b -quark initiated processes (see Figure 4) dominate the production rate by far, while for larger m_A this role is taken over by the loop-induced processes (see Figs. 1 to 3). Accordingly, we split our discussion into the high- m_A and low- m_A cases.

4.2.1 High m_A

The influence of rather light, yet not excluded, superpartners on the total hadronic cross section has been demonstrated to be strong [12]. In particular for the $m_h^{\text{max}}(400)$ scenario with $M_{\text{SUSY}} = 400 \text{ GeV}$ the MSSM cross section for $m_A > 200 \text{ GeV}$ and any $\tan\beta \in [1, 50]$ is reduced by about 20 – 40% compared to the SM. Here, we investigate the impact on the shape of the differential distributions with respect to the SM.

No-mixing(700) scenario:

Figure 5 displays the results for the no-mixing(700) scenario. The lower left panel shows $d\sigma/d\eta_3$ for the MSSM and SM process and also for the three types of subprocesses contributing to h^0 +jet production individually. The typical two-peak shape of the quark-gluon scattering contribution is caused by the harder momentum distribution of up- and down-type quarks with respect to their anti-particles, which lead to a net boost in the direction of motion of the proton providing the quark, still visible in the sum over all partons. The gluon-fusion and the small $q\bar{q}$ contribution are peaked around $\eta_3 = 0$.

The upper left panel of Figure 5 shows the relative difference, δ , between the MSSM and SM prediction for $d\sigma/d\eta_3$. While the total hadronic cross section in the MSSM is enhanced by about 6% compared to the SM, the enhancement of $d\sigma/d\eta_3$ varies only by about 1.3% (between 5.2% and 6.5%) in the range $|\eta_3| < 4.5$.

The right panels in Figure 5 show $d\sigma/dp_T$ for the MSSM and SM processes and the corresponding relative difference, δ . The thickness of the lines in the lower right panel hides the few-percent deviations between MSSM and SM for the important contributions from gluon-fusion and quark-gluon scattering. Interestingly, the deviation between MSSM and SM is largest for $q\bar{q}$ scattering, e.g. 14% for $p_T = 50 \text{ GeV}$. The relative difference in $d\sigma/dp_T$ between the MSSM and the SM (Figure 5, upper right panel) varies between 3% for $p_T = 50 \text{ GeV}$ and 8% (17%) for $p_T = 500 \text{ GeV}$ (1 TeV)

The relative difference between the MSSM and SM prediction for the two-fold differential cross section $d^2\sigma/dp_T/d\eta_3$, indicated by the contours in Figure 10(a), shows a

quantity	no-mixing(700)		$m_h^{\max}(400)$		small α_{eff}	
	SM	MSSM	SM	MSSM	SM	MSSM
σ_c	1.623 pb	1.762 pb	1.448 pb	1.096 pb	1.490 pb	1.356 pb
σ_f	1.682 pb	1.749 pb	1.419 pb	1.031 pb	1.480 pb	1.299 pb
$R = \sigma_c/\sigma_f$	0.965	1.008	1.020	1.063	1.007	1.044
Δ	4.5%		4.2%		3.7%	

Table 1: Cross section predictions for Higgs + jet production with jets radiated into the central (σ_c) and forward part of the detector (σ_f), together with their ratio R and the relative difference between the MSSM and SM value for R , Δ .

non-trivial behaviour with an overall variation of more than 6% in the depicted range, $|\eta_3| < 4.5$ and $30 \text{ GeV} < p_T < 500 \text{ GeV}$. The differently shaped dots in Figure 10(a) show the absolute difference between MSSM and SM, which gives an idea of the kinematical region where the LHC experiments may become sensitive to this difference.

Modifying the cuts may increase the sensitivity to deviations from the SM. Guided by Figure 10, we study the cross section σ_f with rather soft forwardish jets and σ_c with harder more central jets:

$$\sigma_c = \sigma(pp \rightarrow h^0 + \text{jet} + X) |_{|\eta| < 1.5, p_T > 70 \text{ GeV}}, \quad (30)$$

$$\sigma_f = \sigma(pp \rightarrow h^0 + \text{jet} + X) |_{1.5 < |\eta| < 4.5, 30 \text{ GeV} < p_T < 50 \text{ GeV}}. \quad (31)$$

The results are put together in Table 1, where also the ratio

$$R = \frac{\sigma_c}{\sigma_f}. \quad (32)$$

and the relative difference between MSSM and SM

$$\Delta = \frac{R_{\text{MSSM}} - R_{\text{SM}}}{R_{\text{SM}}} \quad (33)$$

are listed. While each individual cross section in the MSSM and the SM is still of the order of 1 pb, which translates into 10^5 raw events for an integrated luminosity of 100 fb^{-1} , the MSSM ratio R_{MSSM} differs by 4.5% compared to R_{SM} .

$m_h^{\max}(400)$ scenario:

Figure 6 contains $d\sigma/d\eta_3$ and $d\sigma/dp_T$ for the $m_h^{\max}(400)$ scenario and the corresponding relative differences to the SM prediction. The total hadronic cross section in this MSSM scenario is about 25% smaller than in the SM. Yet, as far as the η_3 and p_T dependent differences between MSSM and SM are concerned, the same qualitative picture appears. The variation of the relative difference δ with η_3 in the range $|\eta_3| < 4.5$ is about 2% and with p_T in the range $p_T \in [30 \text{ GeV}, 1000 \text{ GeV}]$ is about 7%.

Similar to the no-mixing(700) scenario, the difference in the doubly differential cross section in Figure 10(b) has a non-trivial η_3 and p_T dependence. This suggests a similar

refinement as in the no-mixing(700) scenario. For simplicity, we calculate the same ratio of cross sections according to the same cuts as before (see Eqs. (30) to (32)) for the SM and MSSM. Table 1 shows $\Delta = 4.2\%$ as the relative difference of the ratios.

Small- α_{eff} scenario:

In Figure 7, $d\sigma/d\eta_3$ and $d\sigma/dp_T$ for the small- α_{eff} scenario and corresponding relative differences to the SM are shown. While the total hadronic cross section in this scenario is about 11% below the SM, the variation in the η_3 distribution is about 2%, as in the other two scenarios. Opposite to the other two scenarios the p_T spectrum is slightly softer than in the SM. The range of variation of $d\sigma/dp_T$ with p_T is about 15%.

The doubly differential cross section in Figure 10(c) shows a behaviour similar to the other two scenarios. Calculating the cross section ratio R according to Eqs. (30) to (32) we get $\Delta = 3.7\%$ (see Table 1).

4.2.2 Low m_A

As an example for the low- m_A case at the LHC we show results for the $m_h^{\text{max}}(400)$ scenario in Figure 8. The change with respect to the SM is dramatic. Due to the enhanced cross sections of the b -quark processes, the quark-gluon scattering contribution dominates the cross section and even the contribution from $q\bar{q}$ is larger than from gluon fusion. The total hadronic cross section in the MSSM is 22 times higher than in the SM (≈ 175 pb).

Out of all jets allowed by our cuts (11) a larger fraction of jets is radiated into the central part of the detector. For instance, the fraction of jets produced with $|\eta_3| < 2$ compared to all jets allowed by the cuts is 93% in the MSSM versus 85% in the SM. Correspondingly, the p_T spectrum is much softer than in the SM, yielding an enhanced rate for processes with jet transverse momenta below 850 GeV, e.g. by a factor of 10 for $p_T = 100$ GeV, and rates similar to the SM above 850 GeV.

4.3 Differential cross sections at the Tevatron

The typical hadronic cross section for Higgs + jet in the SM expected at the Tevatron for the cuts $p_T > 30$ GeV and $|\eta_3| < 4.5$ is around 0.1 pb for Higgs masses around 100 GeV, which is possibly not sufficient to be observable at the Tevatron. Therefore, for the Tevatron only the MSSM scenarios with low m_A and $\tan\beta$ not too small are of interest. Those scenarios exhibit a cross section enhanced by a factor of up to 30 compared to the SM [12]. This is due to the contribution of b -quark initiated processes which become dominant because of the strongly enhanced Yukawa coupling of b -quarks to the Higgs boson h^0 .

Figure 9 shows results for the same low- m_A scenario as just described for the LHC in the previous paragraph. Very similar to the LHC case, we see a strongly enhanced total hadronic cross section with a softer p_T spectrum and a larger fraction of jets radiated into the central part of the detector than in the SM.

5 Conclusions

We have calculated pseudorapidity and transverse momentum distributions for the MSSM $h^0 + \text{high-}p_T$ jet production cross section at the LHC and the Tevatron. For scenarios with large m_A , the loop-induced processes dominate the cross section, and superpartners can have a significant impact when they are not too heavy. For small m_A , the Yukawa couplings of the b -quarks are enhanced and hence the cross section is dominated by b -quark induced tree-level parton reactions. The example investigated here, the $m_h^{\text{max}}(400)$ scenario, shows a strongly enhanced hadronic cross section compared to the SM, by a factor of more than 20. Such a scenario predicts for both LHC and Tevatron a softer p_T spectrum, with a fraction of jets radiated into the central part of the detector larger than in the SM.

Acknowledgement

This work was supported in part by the European Community's Marie-Curie Research Training Network under contract MRTN-CT-2006-035505 'Tools and Precision Calculations for Physics Discoveries at Colliders' (HEPTOOLS).

References

- [1] CMS Physics Technical Design Report, Vol. II, CERN/LHCC 2006-021.
- [2] R. K. Ellis, I. Hinchliffe, M. Soldate and J. J. van der Bij, Nucl. Phys. B **297** (1988) 221; U. Baur and E. W. Glover, Nucl. Phys. B **339** (1990) 38; M. Chaichian, I. Liede, J. Lindfors and D. P. Roy, Phys. Lett. B **198** (1987) 416 [Erratum-ibid. B **205** (1987) 595].
- [3] S. Abdullin, M. Dubinin, V. Ilyin, D. Kovalenko, V. Savrin and N. Stepanov, Phys. Lett. B **431** (1998) 410.
- [4] V. V. Zmushko, ATL-PHYS-2002-020, IHEP-2002-23.
- [5] B. Mellado, W. Quayle and S. L. Wu, Phys. Lett. B **611** (2005) 60.
- [6] C. Anastasiou, K. Melnikov and F. Petriello, Phys. Rev. Lett. **93** (2004) 262002, Nucl. Phys. B **724** (2005) 197.
- [7] G. Bozzi, S. Catani, D. de Florian and M. Grazzini, Phys. Lett. B **564** (2003) 65; S. Catani, D. de Florian, M. Grazzini and P. Nason, JHEP **0307** (2003) 028.
- [8] D. de Florian, M. Grazzini and Z. Kunszt, Phys. Rev. Lett. **82** (1999) 5209.
- [9] D. de Florian, A. Kulesza and W. Vogelsang, JHEP **0602** (2006) 047.
- [10] B. Field, S. Dawson and J. Smith, Phys. Rev. D **69** (2004) 074013.
- [11] U. Langenegger, M. Spira, A. Starodumov and P. Trueb, hep-ph/0604156.
- [12] O. Brein and W. Hollik, Phys. Rev. D **68** (2003) 095006.
- [13] O. Brein and W. Hollik, Eur. Phys. J. C **13** (2000) 175; O. Brein, W. Hollik and S. Kanemura, Phys. Rev. D **63** (2001) 095001.
- [14] R. Brock *et al.* [CTEQ Collaboration], *Handbook of perturbative QCD: Version 1.0*, Rev. Mod. Phys. **67** (1995) 157.
- [15] A. D. Martin, R. G. Roberts, W. J. Stirling and R. S. Thorne, Phys. Lett. B **604** (2004) 61.
- [16] R. V. Harlander and W. B. Kilgore, Phys. Rev. D **68** (2003) 013001.
- [17] D. Rainwater, M. Spira and D. Zeppenfeld, hep-ph/0203187; F. Maltoni, Z. Sullivan and S. Willenbrock, Phys. Rev. D **67** (2003) 093005; E. Boos and T. Plehn, hep-ph/0304034.
- [18] W. M. Yao *et al.* [Particle Data Group], J. Phys. G **33** (2006) 1.

- [19] M. Carena, S. Heinemeyer, C. E. M. Wagner and G. Weiglein, Eur. Phys. J. C **26** (2003) 601.
- [20] S. Schael *et al.* [ALEPH Collaboration], Eur. Phys. J. C **47**, 547 (2006).
- [21] S. Heinemeyer, W. Hollik and G. Weiglein, Eur. Phys. J. C **9** (1999) 343 and Comput. Phys. Commun. **124**, 76 (2000);
G. Degrossi, S. Heinemeyer, W. Hollik, P. Slavich and G. Weiglein, Eur. Phys. J. C **28** (2003) 133;
M. Frank, T. Hahn, S. Heinemeyer, W. Hollik, H. Rzehak and G. Weiglein, hep-ph/0611326.
- [22] A. L. Kagan and M. Neubert, Phys. Rev. D **58** (1998) 094012 and Eur. Phys. J. C **7** (1999) 5;
The code we are using is taken from T. Hahn, W. Hollik, J. I. Illana and S. Peñaranda, hep-ph/0512315.
- [23] S. Chen *et al.* [CLEO Collaboration], Phys. Rev. Lett. **87** (2001) 251807;
B. Aubert *et al.* [BABAR Collaboration], hep-ex/0207074;
E. Barberio *et al.* [Heavy Flavor Averaging Group (HFAG)], hep-ex/0603003.
- [24] M. Misiak *et al.*, Phys. Rev. Lett. **98** (2007) 022002.
- [25] S. Heinemeyer, W. Hollik and G. Weiglein, Phys. Rept. **425**, 265 (2006).

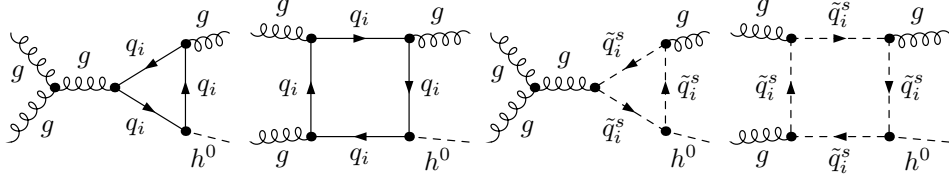


Figure 1: Typical quark and squark loop graphs for the process $gg \rightarrow gh^0$ in leading order. Feynman graphs with opposite direction of charge flow are not depicted.

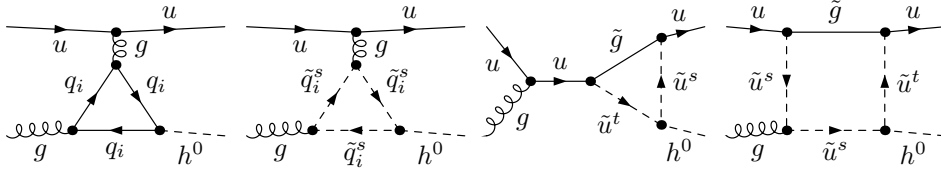


Figure 2: Typical Feynman graphs for the process $ug \rightarrow uh^0$ in leading order. For the scattering of the other quarks (d, c, s) the graphs look similar.

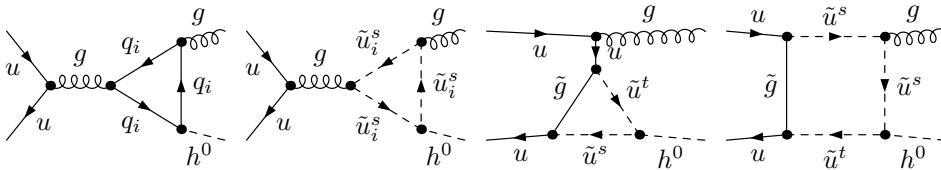


Figure 3: Typical Feynman graphs for the process $u\bar{u} \rightarrow gh^0$ in leading order. For the scattering of the other quarks (d, c, s) the Feynman graphs look similar.

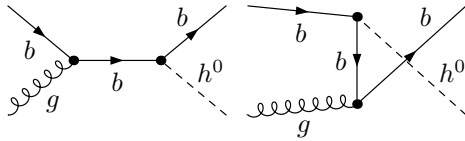


Figure 4: Feynman graphs for the b -quark processes in leading order. The graphs represent the amplitude for the process $bg \rightarrow bh^0$ if the time axis points to the right and $b\bar{b} \rightarrow gh^0$ if it points down.

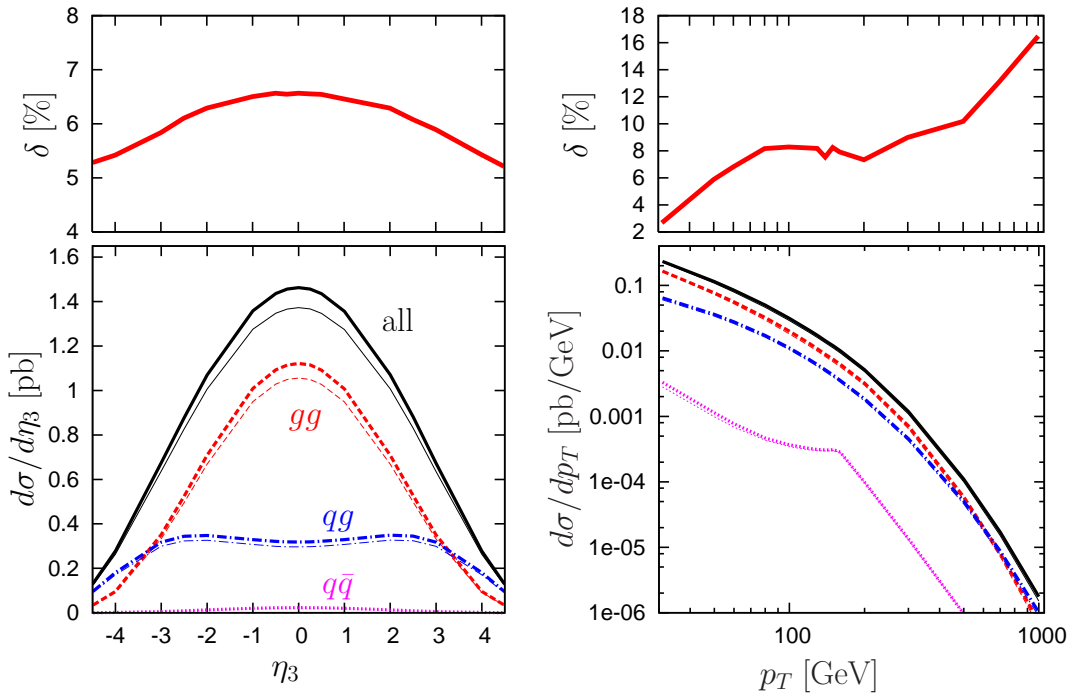


Figure 5: LHC, no-mixing(700) scenario with $m_{A^0} = 500$ GeV, $\tan\beta = 35$: hadronic cross section for Higgs + jet production differential in the jet's pseudorapidity η_3 and transverse momentum p_T (lower left and right panel). Thick and thin lines indicate the MSSM and SM predictions respectively. Solid lines indicate the full result, dashed, dot-dashed and dotted lines the gg -, qg - and $q\bar{q}$ contribution respectively. In the upper panels the relative difference between the MSSM and SM result is displayed.

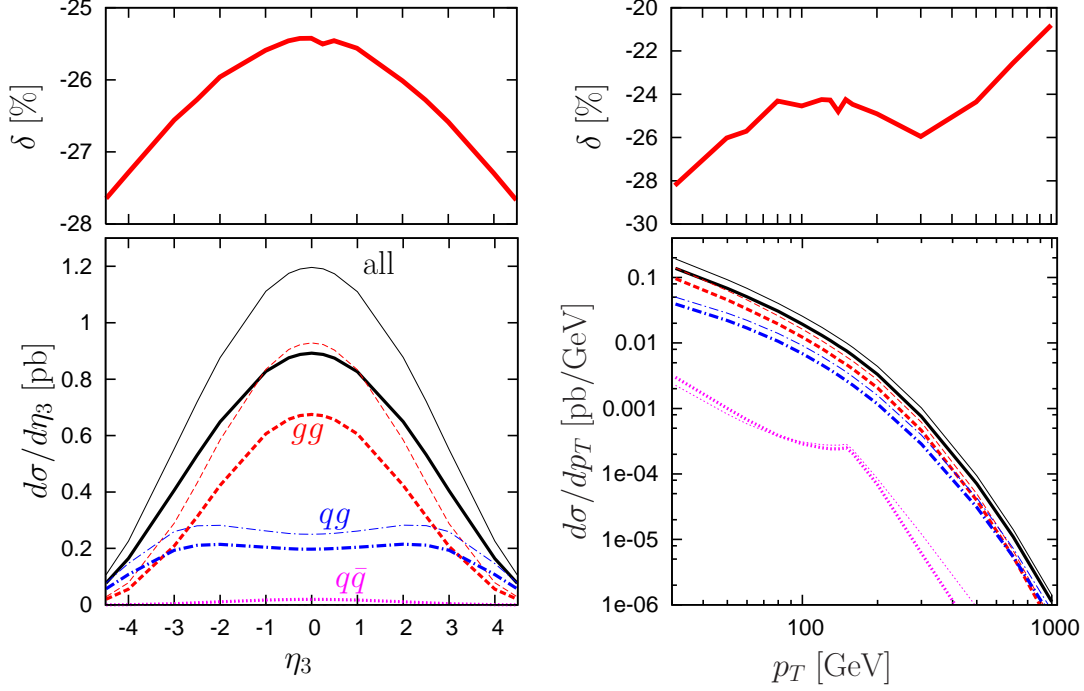


Figure 6: LHC, mh-max scenario with $m_{A^0} = 400$ GeV, $\tan \beta = 30$: differential hadronic cross sections for Higgs + jet production . See caption of Figure 5 for more details.

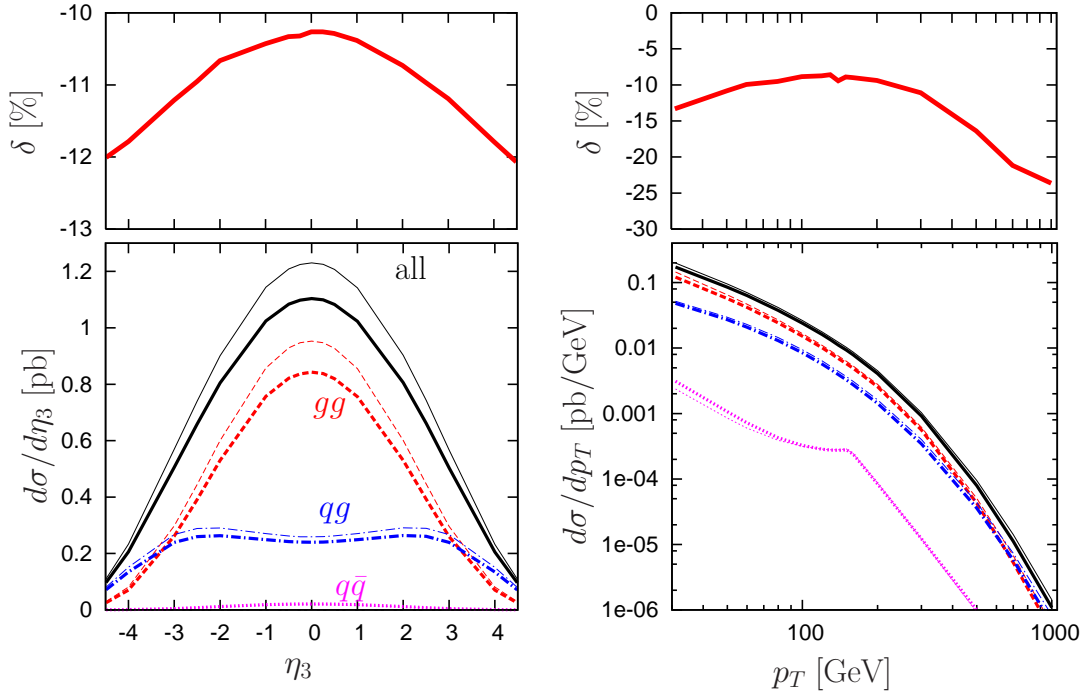


Figure 7: LHC, small alpha-eff scenario with $m_{A^0} = 400$ GeV, $\tan \beta = 30$: differential hadronic cross sections for Higgs + jet production. See caption of Figure 5 for more details.

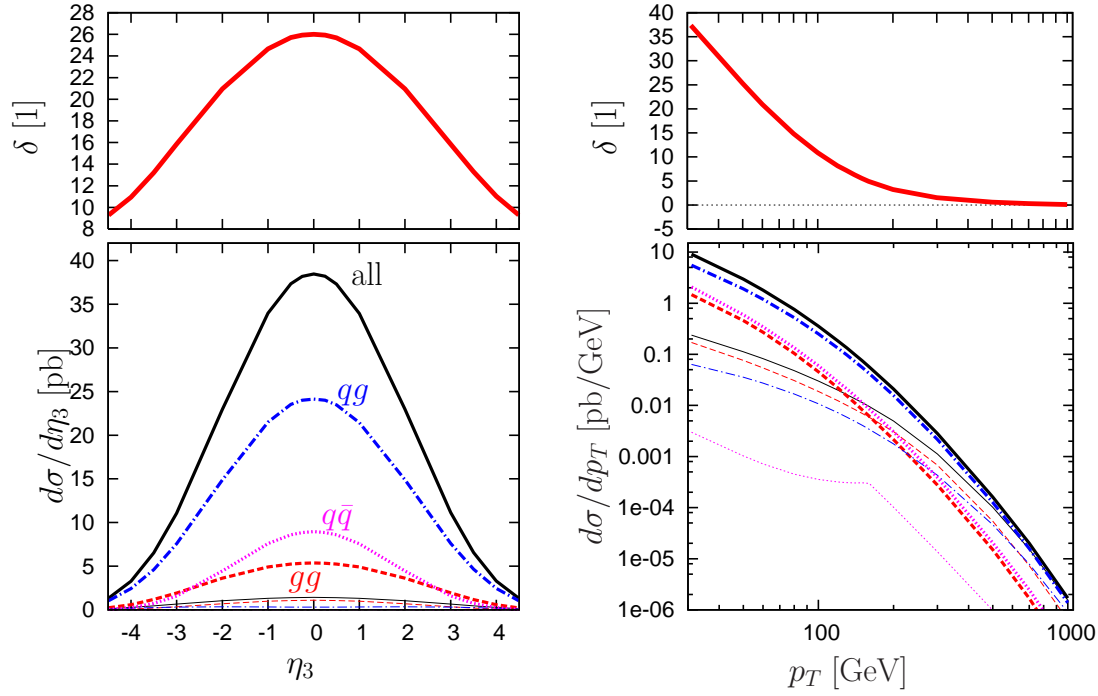


Figure 8: LHC, mh-max scenario with $m_{A^0} = 110$ GeV, $\tan\beta = 30$: differential hadronic cross sections for Higgs + jet production. See caption of Figure 5 for more details.

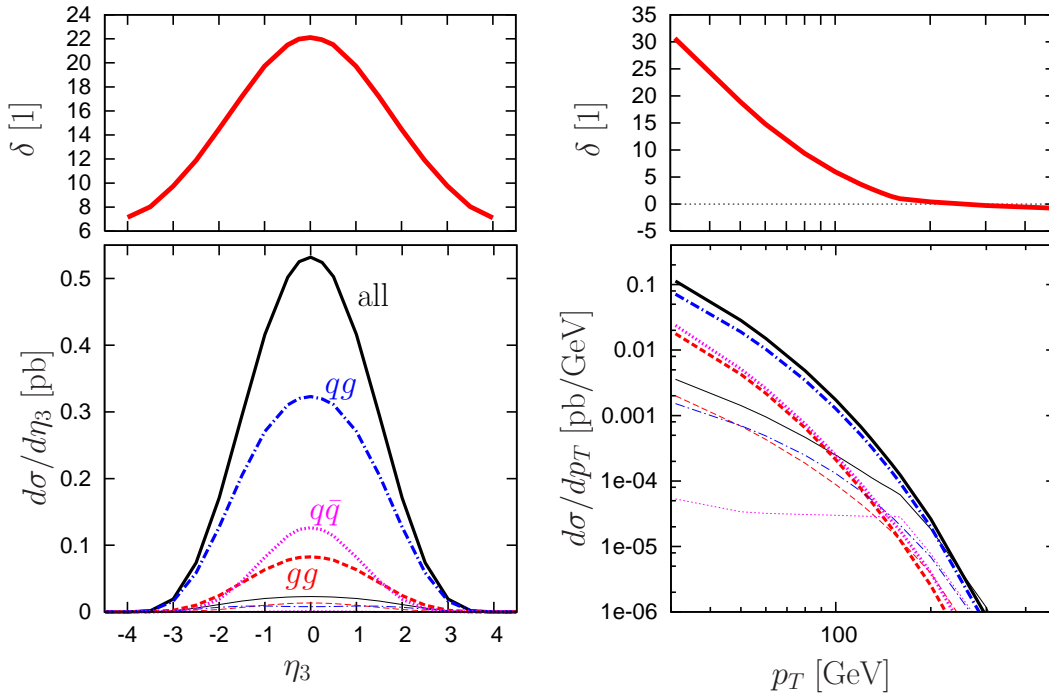


Figure 9: Tevatron, mh-max scenario with $m_{A^0} = 110$ GeV, $\tan\beta = 30$: differential hadronic cross sections for Higgs + jet production. See caption of Figure 5 for more details.

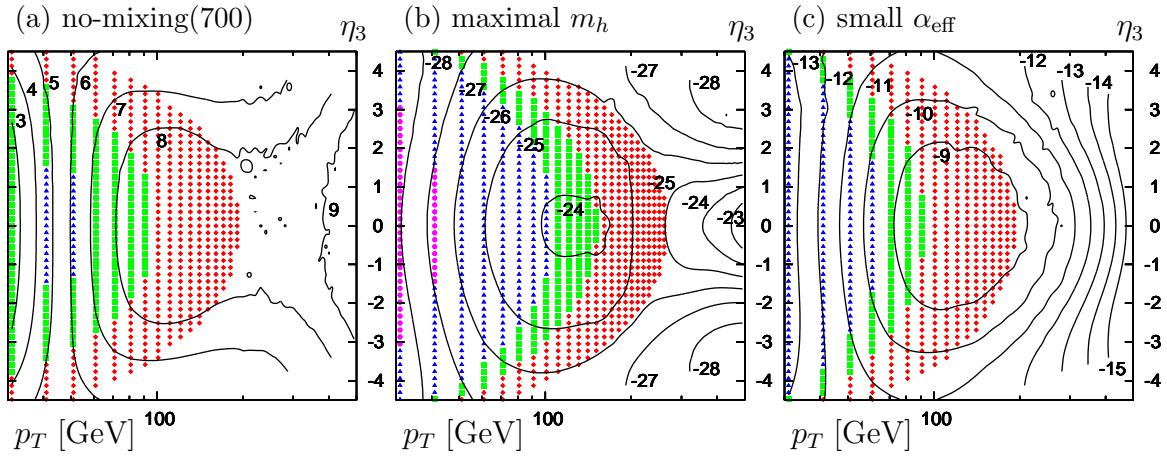


Figure 10: Relative and absolute difference between the MSSM and SM prediction for $d^2\sigma/d\eta_3 dp_T$ at the LHC for the three benchmark scenarios as a function of p_T and η_3 . The contour lines show the relative difference of the predictions in percent, while diamonds (\blacklozenge), squares (\blacksquare), triangles (\blacktriangle), circles (\bullet), refer to an absolute difference in the range 0.1-0.5 fb/GeV, 0.5-1 fb/GeV, 1-5 fb/GeV, 5-10 fb/GeV respectively. In the white area the difference is less than 0.1 fb/GeV.